Check for updates

How to cite: *Angew. Chem. Int. Ed.* **2024**, *63*, e202410097
doi.org/10.1002/anie.202410097

VIP COFs for Catalysis Very Important Paper

Tailoring Catalysis of Encapsulated Platinum Nanoparticles by Pore Wall Engineering of Covalent Organic Frameworks

*Mingchun Guo[+], Xinyu Guan[+], Qiangqiang Meng, Ming-Liang Gao, Qunxiang Li, and Hai-Long Jiang**

Abstract: While supported metal nanoparticles (NPs) have shown significant promise in heterogeneous catalysis, precise control over their interaction with the support, which profoundly impacts their catalytic performance, remains a significant challenge. In this study, Pt NPs are incorporated into thioether-functionalized covalent organic frameworks (denoted COF-S_x), enabling precise control over the size and electronic state of Pt NPs by adjusting the thioether density dangling on the COF pore walls. Notably, the resulting Pt@COF-S_x demonstrate exceptional selectivity (> 99 %) in catalytic hydrogenation of *p*-chloronitrobenzene to *p*-chloroaniline, in sharp contrast to the poor selectivity of Pt NPs embedded in thioether-free COFs. Furthermore, the conversion over Pt@COF-S_x exhibits a volcano-type curve as the thioether density increases, due to the corresponding change of accessible Pt sites. This work provides an effective approach to regulating the catalysis of metal NPs via their microenvironment modulation, with the aid of rational design and precise tailoring of support structure.

Introduction

Highly dispersed metal nanoparticles (NPs) have garnered considerable attention in heterogeneous catalysis, particularly in hydrogenation, oxidation, and coupling reactions, due to their unique electronic characteristics and high surface-to-volume ratio.[1] Nevertheless, their practical application is hindered by their tendency to aggregation, leading to a decline in catalytic performance.[2] To address this issue, researchers have explored various supports, such as metal oxides, graphene, and polymers, to stabilize metal NPs. However, deposition of metal NPs on these solid supports often leads to complex surface structures with limited interface contact, which not only usually gives rise to potential aggregation but also leads to somewhat difficulty in the regulation of metal-support interactions for improved catalysis.[3]

To overcome these limitations, crystalline porous materials (CPMs), such as zeolites, metal–organic frameworks (MOFs) and covalent organic frameworks (COFs), have emerged as promising platforms for the immobilization of metal NPs due to their unique properties.[2a,4] Amongst these materials, COFs,[5] constructed from organic building blocks, offer highly designable frameworks and tailorable functionalities, making them desirable supports. The robust and highly porous structures are able to prevent the aggregation of metal NPs, and the geometric and electronic structures of metal NPs would be significantly affected by multidimensional metal-support interactions with the COF skeleton. This presents a novel strategy to the regulation of catalytic performance of metal NPs, offering an elegant alternative to the conventional methods that directly modify and/or tune the parameters of metal NPs, such as particle size, morphology, loading amount, alloying, etc.[6] Furthermore, COFs offer well-defined structures, allowing precise control of the microenvironment around metal NPs by grafting specific functional groups onto their pore walls.[7] Given the above merits, as a matter of fact, there have been limited examples on the incorporation of metal NPs, such as Au, Pd, and Pt NPs, into COFs,[8] where the investigations are basically related to the stabilization of metal NPs with small sizes or their electronic state regulation by functional groups on the COFs (with one example only[8e]). However, to the best of our knowledge, it remains largely unexplored for the simultaneous confinement and electronic structure regulation of metal NPs gained by the manipulation of the host COF structures.

With this in mind, a series of thioether-functionalized COFs (denoted as COF-S_x) with the same topology and similar skeletons yet varying thioether contents have been designed and synthesized to immobilize Pt NPs, affording Pt@COF-S_x composites (Scheme 1). Remarkably, the particle sizes and electronic properties of Pt NPs can be systematically tailored by adjusting the density of thioether on the COF pore walls. As a result, these Pt NPs embedded in thioether-functionalized COFs demonstrate high selectivity (> 99 %) in the hydrogenation of *p*-chloronitrobenzene

[*] M. Guo,[+] Dr. X. Guan,[+] Dr. M.-L. Gao, Prof. Dr. H.-L. Jiang
Hefei National Research Center for Physical Sciences at the Microscale, Department of Chemistry
University of Science and Technology of China, Hefei, Anhui 230026 (P. R. China)
E-mail: jianglab@ustc.edu.cn
Homepage: http://mof.ustc.edu.cn/

Dr. Q. Meng, Prof. Dr. Q. Li
Department of Chemical Physics, University of Science and Technology of China, Hefei, Anhui 230026 (P. R. China)

Dr. X. Guan[+]
Hangzhou Institute of Advanced Studies, Zhejiang Normal University, Hangzhou, Zhejiang 310000 (P. R. China)

[+] These authors contributed equally to this work.

© 2024 Wiley-VCH GmbH

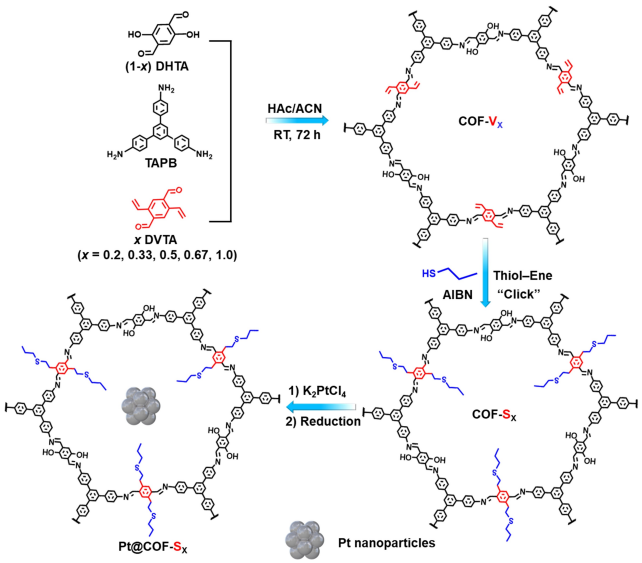

Scheme 1. Illustration of the synthetic route to Pt@COF-S_x composites.

(*p*-CNB) to *p*-chloroaniline (*p*-CAN), surpassing the selectivity achieved with Pt NPs in thioether-free COFs (*p*-CAN selectivity of 53–87 %). Moreover, the hydrogenation activity exhibits a distinctive trend, forming a volcano curve along with the increase in thioether density within the COF pores, which can be attributed to the change of accessible Pt sites. To the best of our knowledge, this represents the first report on regulating the size and electronic structure of incorporated metal NPs by tailoring functional moieties on the COF supports.

Results and Discussion

The synthesis of Pt@COF-S_x composites involves a multistep procedure (Scheme 1). Initially, the parent vinyl-functionalized COF-V_x were crystallized by a mixed-linker methodology, featuring a uniform arrangement of variable proportions of vinyl moieties within similar COF skeletons.[9] This synthesis procedure involves 1,3,5-tri(4-aminophenyl)benzene (TAPB) as the tritopic monomer, with 2,5-dihydroxyterephthaldeyde (DHTA) and 2,5-divinylterephthalaldehyde (DVTA) serving as the edge units. The degree of vinyl functionalization is denoted by the molar ratio of DVTA relative to the overall edge linkers, which can be calculated as $x = [DVTA]/([DVTA]+[DHTA])$. Subsequently, the COF-$V_x$ materials were converted into the corresponding COF-S_x materials through a stoichiometric thiol-ene click reaction involving 1-propanethiol.[10] Finally, Pt NPs were incorporated into the COF-S_x through solution impregnation followed by reduction in H_2 atmosphere, resulting in the fabrication of Pt@COF-S_x composites.

Powder X-ray diffraction (XRD) patterns reveal the AA-stacked boron nitride nets (bnn) with hexagonal channels for COF-V_x (Figure S1), while the completely disappearance of diffraction peaks from the monomers indicates the successful polymerization process (Figure S2). Similar powder XRD patterns are observed for COF-V_x, COF-S_x and Pt@COF-S_x, indicating that the incorporation of pendant moieties on the skeleton and the guest metal NPs do not influence the COF structure of skeleton (Figure 1a, S1 and S3). Solid-state ^{13}C cross-polarization magic-angle-spinning nuclear magnetic resonance (ssNMR) and Fourier transform infrared (FT-IR) spectra have been further conducted to confirm the successful preparation and modification of the COFs (Figure S4–S7). The formation of imine linkages is validated by the characteristic chemical shift at ~157 ppm in ssNMR spectra and IR peak at ~1614 cm^{-1} (Figure S4 and S5). Moreover, the newly formed signals between 10–40 ppm and methylene IR adsorption peaks at approximately 2929 cm^{-1} support the occurrence of the thiol-ene click reaction (Figure S6 and S7).

Nitrogen sorption isotherms recorded at 77 K exhibit similar type IV isotherms, revealing the mesoporous characteristics of these COFs. A slight decline is observed for the N_2 sorption amount, corresponding to the gradually reduced Brunauer–Emmett–Teller (BET) surface areas, from 606–913 $m^2 g^{-1}$ for COF-V_x to 319–529 $m^2 g^{-1}$ for COF-S_x and 234–508 $m^2 g^{-1}$ for Pt@COF-S_x, respectively. This decline is possibly due to the additional mass and pore occupation originating from the post-incorporated pendant groups and Pt NPs (Figure 1b, S8–S10 and Table S1). Moreover, the BET surface area displays a diminishing trend as the *x* value increases for each set of COF-V_x, COF-S_x or Pt@COF-S_x, which is reasonable as the COF pores would be occupied with increasing density of pendant groups. The ^1H NMR spectra are adopted to determine the vinyl contents in COF-

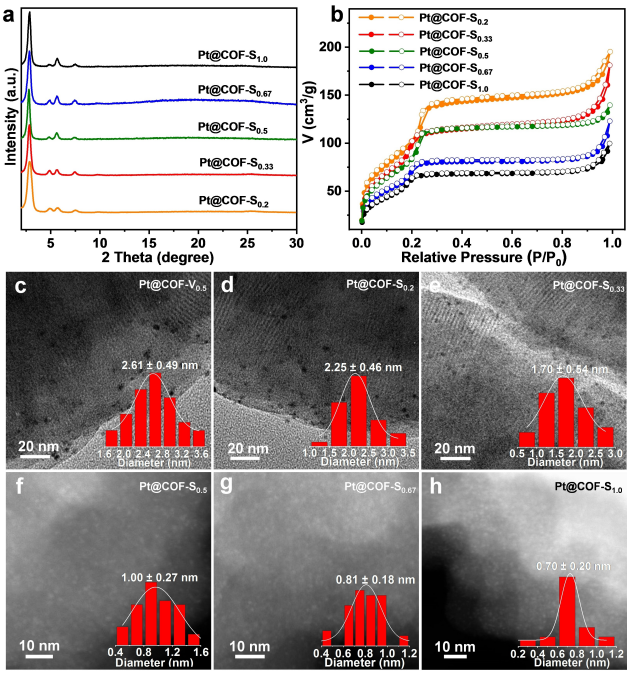

Figure 1. a) Powder XRD patterns and b) nitrogen sorption isotherms of Pt@COF-S_x composites at 77 K. TEM images of c) Pt@COF-$V_{0.5}$, d) Pt@COF-$S_{0.2}$ and e) Pt@COF-$S_{0.33}$. HAADF-STEM images of f) Pt@COF-$S_{0.5}$, g) Pt@COF-$S_{0.67}$ and h) Pt@COF-$S_{1.0}$. Inset: size distributions of Pt NPs.

© 2024 Wiley-VCH GmbH

15213773, 2024, 39, Downloaded from https://onlinelibrary.wiley.com/doi/10.1002/anie.202410097 by University Of Science, Wiley Online Library on [17/09/2024]. See the Terms and Conditions (https://onlinelibrary.wiley.com/terms-and-conditions) on Wiley Online Library for rules of use; OA articles are governed by the applicable Creative Commons License

V_x, which are almost consistent with the theoretical values (Table S2). The contents of Pt and S elements have been determined using inductively coupled plasma-optical emission spectrometry (ICP-OES) and CHNS elemental analyses, respectively. As expected, the Pt contents are almost consistent (1.8 ± 0.1 wt %) across all Pt@COF-S_x composites, while the S contents display an ascending trend correlating with the increase in the *x* value from 0.2 to 1.0 (Table S3). Scanning electron microscopy (SEM) images display similar spherical morphologies for Pt@COF-S_x composites, with approximate diameters of 500 nm (Figure S11). Transmission electron microscopy (TEM) observations suggest the apparent reduction in sizes of Pt NPs along with an increase of thioether density, as evidenced by the Pt sizes of ~2.61 nm for thioether-free Pt@COF-$V_{0.5}$, ~2.25 nm for Pt@COF-$S_{0.2}$ and ~1.70 nm for Pt@COF-$S_{0.33}$, respectively (Figure 1c–e). However, as the thioether content is further increased, the reduced sizes of Pt NPs pose challenges in visual identification through TEM images (Figure S12). To address this issue, high-angle annular dark-field scanning transmission electron microscopy (HAADF-STEM) has been adopted to examine these subnanometric Pt particles. The results support the comparable or slightly reduced Pt sizes of ~1.00 nm, ~0.81 nm and ~0.70 nm for Pt@COF-$S_{0.5}$, Pt@COF-$S_{0.67}$ and Pt@COF-$S_{1.0}$, respectively (Figure 1f–h). In addition, elemental mapping displays the uniform distribution of Pt species throughout the Pt@COF-$S_{0.5}$ composite as a representative (Figure S13). Moreover, thermogravimetric analysis (TGA) reveals remarkable thermal stability of all Pt@COF-S_x composites, which can remain stable up to ~300 °C with negligible weight loss under nitrogen atmosphere (Figure S14).

To investigate the interaction between the COF skeletons and the encapsulated Pt NPs, X-ray photoelectron spectroscopy (XPS) measurements have been executed. In comparison to the binding energy of Pt $4f_{7/2}$ at 71.38 eV for thioether-free Pt@COF-$V_{0.5}$, the peak for Pt@COF-S_x shifts to higher values, varying from 71.45 eV to 71.72 eV (Figure 2a).[11] Moreover, with the increase in the value of *x* in Pt@COF-S_x, there is a noticeable upwards trend in the binding energy of Pt $4f_{7/2}$, accompanied by a corresponding downwards trend in the S 2p binding energy (Figure S15). Notably, almost no visible binding energy shift for the O 1s is observed (Figure S16). These results indicate an amplified electron-deficient nature of Pt and a greater negative charge accumulation on S with the increasement of thioether density within the skeleton, suggesting electron transfer from Pt NPs to the S moieties but not to the hydroxyl group. To further clarify the alterations of surface Pt electronic states, diffuse reflectance infrared Fourier transform spectroscopy (DRIFTS) has been adopted using CO as the probe molecule, in which a blue-shifted CO vibration typically indicates more positively charged Pt surfaces with enhanced interactions with CO molecules. For all these COF-confined Pt NPs, typical peaks are observed within the region of 2060 to 2100 cm^{-1}, referring to the linear mode of CO binding. In comparison to the 2060 cm^{-1} observed in thioether-free Pt@COF-$V_{0.5}$, the CO vibration undergoes significant blue-shift upon thioether functionalization, and this effect becomes more pronounced with higher thioether density, ranging from 2068 cm^{-1} for Pt@COF-$S_{0.2}$ to 2100 cm^{-1} for Pt@COF-$S_{1.0}$, indicating gradually increased positive charge on the Pt surface with the increasement of thioether group within the skeleton (Figure 2b).[8e,12] In brief, the results from XPS and CO-DRIFTS collectively demonstrate an increased electron-deficient nature of the Pt surfaces through thioether modification onto the COF pore walls.

Encouraged by the control of sizes and electronic state for Pt NPs induced by pendant group engineering on the COF pore walls, selective hydrogenation of *p*-CNB has been investigated.[13] All Pt@COF-S_x catalysts, encompassing various *x* values, demonstrate consistently high selectivity (> 99 %) to *p*-CAN (Figure 3a), the expected value-added product. By sharp contrast, Pt NPs loaded into thioether-free COFs, such as Pt@COF-V_0, Pt@COF-$V_{0.5}$, and Pt@COF-$V_{1.0}$, exhibit much reduced *p*-CAN selectivity, ranging from 53 % to 87 %, accompanied by the emergence of dechlorinated byproducts (Figure 3b). Notably, the im-

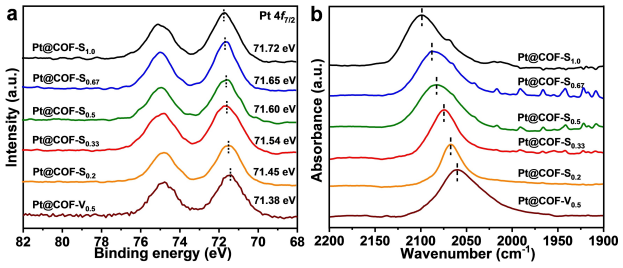

Figure 2. a) XPS spectra of Pt $4f_{7/2}$ and b) CO-DRIFTS spectra at 298 K for Pt@COF-S_x composites.

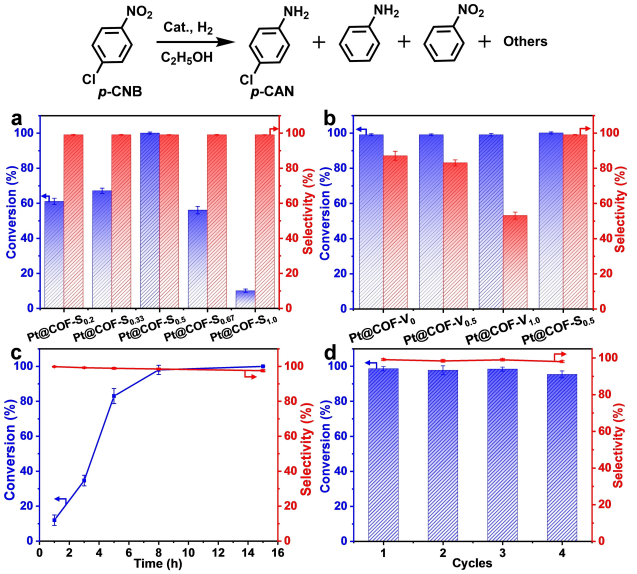

Figure 3. The conversion of *p*-CNB and selectivity to *p*-CAN over a) Pt@COF-S_x and b) Pt@COF-V_x. c) Time-dependent conversion and selectivity over Pt@COF-$S_{0.5}$. d) Recycling performance of Pt@COF-$S_{0.5}$ in the selective hydrogenation of *p*-CNB. Error bar represents standard deviation based on three replicates.

© 2024 Wiley-VCH GmbH

15213773, 2024, 39, Downloaded from https://onlinelibrary.wiley.com/doi/10.1002/anie.202410097 by University Of Science, Wiley Online Library on [17/09/2024]. See the Terms and Conditions (https://onlinelibrary.wiley.com/terms-and-conditions) on Wiley Online Library for rules of use; OA articles are governed by the applicable Creative Commons License

pressive selectivity of Pt@COF-S_x can be maintained even when extending the reaction time to 15 hours, underscoring the persistent inhibition of the dehalogenation pathway (Figure 3c). Moreover, the Pt@COF-S_x composites display a distinct volcano-like profile concerning the *p*-CNB conversion along with increasing *x* values from 0.2 to 1.0, attaining maximum conversion (> 99 %) by Pt@COF-$S_{0.5}$ with $x = 0.5$ (Figure 3a). This observation highlights the significant role of the thioether microenvironment around Pt NPs toward the control of selectivity and conversion during the hydrogenation process. Given the negligible conversion observed over COF-$S_{0.5}$ or in the absence of catalyst (Table S4, entries 1 and 2), Pt NPs are assumed to be the real active sites for the hydrogenation reaction. As controls, Pt/C and Pt/Al_2O_3, as common supported Pt catalysts, display *p*-CAN selectivity as low as 41 % and 53 %, respectively, indicating the concurrent dichlorination process (Table S4, entries 3 and 4). These results clearly demonstrate that Pt@COF-S_x display much superior selectivity to *p*-CAN over those traditional Pt catalysts, which might be attributed to the created thioether microenvironment around Pt NPs.

Subsequently, recycling experiments have been conducted over the optimal catalyst Pt@COF-$S_{0.5}$, and the results demonstrate the well-maintained activity and selectivity in the four consecutive recycling tests (Figure 3d), manifesting excellent stability and recyclability of the catalyst. Meanwhile, both powder XRD patterns and TEM images can be well preserved after catalysis and even recycling tests (Figure S17–S20), highlighting the excellent stability of the COF skeleton and the retained good dispersion of incorporated Pt NPs. By contrast, the thioether-free Pt@COF-$V_{0.5}$ showcases a significant decay in activity and selectivity under similar reaction conditions, presenting only 60 % conversion and 65 % selectivity at the fourth run (Figure S21). The above comparison emphasizes that the specific microenvironment created by thioether groups within the COF channel not only affects the activity and selectivity of Pt NPs but also possibly plays critical roles in the Pt stability. In addition, a hot filtration experiment displays no further conversion upon the removal of Pt@COF-$S_{0.5}$ and no Pt leaching in the filtrate (Figure S22), unambiguously demonstrating the truly heterogeneous nature of the catalytic process.

In order to further demonstrate the general applicability of Pt@COF-$S_{0.5}$ toward selective hydrogenation, the comprehensive evaluation of various substituted nitrobenzene compounds has been undertaken (Figure S23–S27). To our delight, Pt@COF-$S_{0.5}$ persistently exhibits high selectivity, effectively converting all investigated substrates into the corresponding halogenated aniline products. This indicates its exceptional toleration for the hydrogenation across a diverse range of substituted nitrobenzenes. Notably, fluoro- or chloro-substituted nitrobenzene derivatives can be completely converted within 10 hours (Figure S23–S25), comparable with the 8-hour conversion for *p*-CNB. However, an apparent deceleration in reaction kinetics is observed when the substituents are altered to cyano and bromo groups, extending the reaction time length to 14 and 32 hours, respectively, for full conversion (Figure S26 and S27). The different catalytic hydrogenation rates of substituted nitrobenzenes might be attributed to the electronic effect of the substituent groups, in which the cyano or bromo groups exhibit stronger electron-withdrawing affinity compared to the fluoro and chloro groups.[14] These results not only support the persistently high selectivity of Pt@COF-$S_{0.5}$ but also suggest the significant influence of electronic effect on the reaction kinetics in the selective hydrogenation process.

Then, the DRIFTS spectra of competitive adsorption experiments involving chlorobenzene (CB) and nitrobenzene (NB) are resorted to assess the binding affinity of the $–NO_2$ and –Cl groups, aiming to elucidate the mechanism behind the high selectivity observed for Pt@COF-$S_{0.5}$ (Figure 4). For both Pt@COF-$S_{0.5}$ and Pt@COF-$V_{0.5}$, their DRIFTS spectra present characteristic bands, including the adsorbed nitro groups from NB at 1528 and 1347 cm^{-1} and signals associating with C–Cl bonds from CB at 742 cm^{-1}. After purging with Ar, the DRIFTS for Pt@COF-$S_{0.5}$ displays almost unaltered $–NO_2$ signals but a gradually diminished C–Cl signal, signifying a stronger affinity of NB compared to CB over Pt@COF-$S_{0.5}$. In sharp contrast, the trend is nearly opposite for thioether-free Pt@COF-$V_{0.5}$ upon Ar purging, where C–Cl peak remains consistent while $–NO_2$ signal decreases quickly. These results indicate a more favorable binding interaction of $-NO_2$ in Pt@COF-$S_{0.5}$, offering the explanation for the enhanced selectivity after thioether functionalization on the skeleton.

To further explain the improved selectivity after thioether modification, energy diagrams are calculated to illustrate the reaction mechanism. Initially, the models of neutral or positively charged Pt (111) surfaces have been constructed, simulating Pt NPs incorporated into the skeletons in the absence and presence of pendant thioether groups, respectively, as inspired by the modulated electronic state of Pt NPs based on the above XPS and CO-DRIFTS experimental results (Figure 2). Two conceivable pathways along the reaction coordinate are proposed, including path I corresponding to the formation of *p*-CAN and path II starting with dichlorination reactions.[15] While both pathways are characterized as exothermic processes on Pt surfaces, path I towards the generation of *p*-CAN is thermodynamically favored, given its much lower relative energies compared to path II (Figure S28 and S29). Additionally, the key intermediates in this pathway can be

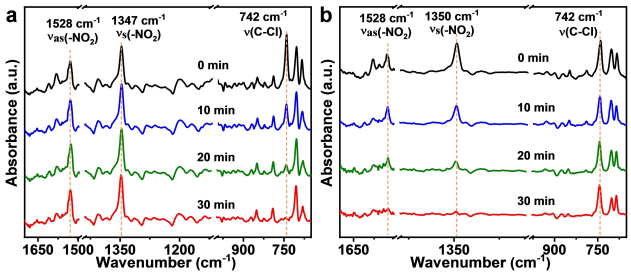

Figure 4. DRIFTS spectra of the mixture of chlorobenzene and nitrobenzene adsorbed onto the Pt sites in a) Pt@COF-$S_{0.5}$ and b) Pt@COF-$V_{0.5}$.

© 2024 Wiley-VCH GmbH

15213773, 2024, 39, Downloaded from https://onlinelibrary.wiley.com/doi/10.1002/anie.202410097 by University Of Science, Wiley Online Library on [17/09/2024]. See the Terms and Conditions (https://onlinelibrary.wiley.com/terms-and-conditions) on Wiley Online Library for rules of use; OA articles are governed by the applicable Creative Commons License

observed from *in situ* DRIFTS analysis over Pt@COF-$S_{0.5}$ (Figure S30). Upon the introduction of H_2, the nitro signals at 1528 and 1347 cm^{-1} gradually diminish, accompanied by the steady emergence of signals at 1507 cm^{-1} and 1362 cm^{-1} corresponding to N=O bond in Ph-NO and N–O bond in Ph-NHOH, respectively. These DRIFTS results suggest Ph-NO and Ph-NHOH as the intermediate species during the hydrogenation of nitrobenzene over Pt@COF-S_x, further evidencing path I as the possible pathway in *p*-CNB hydrogenation.

On the basis of the proposed path I, DFT calculations demonstrate similar exothermic procedures on both neutral and positively charged Pt surface (Figure 5, S29 and S31). However, the key intermediates are more easily generated on the positively charged surface, as evidenced by the significantly lower relative energy (C_6H_4ClNO: −0.69 eV vs. −0.87 eV on neutral or positively charged Pt surface, respectively; $C_6H_4ClNHOH$: −1.05 eV vs. −1.39 eV on neutral or positively charged Pt surface, respectively). In addition, the relative energy of *p*-CAN is also much lower on the positively charged Pt surface (−2.16 eV), compared with −1.49 eV on neutral Pt surfaces, implying that *p*-CAN is more easily generated when the Pt surface is positively charged (Figure 5). Consequently, these DFT results offer reasonable explanations for the significantly improved *p*-CAN selectivity on the positively charged Pt sites in Pt@COF-S_x compared to the neutral Pt sites in Pt@COF-V_x.

Except for high *p*-CAN selectivity for Pt@COF-S_x, the mechanism behind the catalytic activity has also been investigated. Notably, the conversion over Pt@COF-S_x exhibits a volcano-type curve along with the increasing thioether density, different from the increasing positive charges on Pt surfaces. This discrepancy implies the influence caused by other crucial factors, possibly the availability of Pt sites. To examine this point, CO titration experiments have been adopted and the Pt dispersion is calculated based on the CO adsorption amount per mass of sample (Table S5).[16] While Pt@COF-S_x demonstrate almost consistent Pt content (1.8 ± 0.1 wt %), the CO adsorption amount reaches its maximum at $x = 0.5$, indicating optimal accessibility of Pt sites and the highest Pt dispersion of 66.2 % for Pt@COF-$S_{0.5}$. The Pt dispersion increases with rising x in the range of 0.2–0.5, in correlation with gradually reduced Pt sizes in Pt@COF-S_x (Figure 1d–f). However, as the thioether content further increases in Pt@COF-S_x (x = 0.5–1.0), despite almost comparable Pt sizes (Figure 1f–h), an unexpected decrease is observed for accessible Pt sites. This is possibly attributed to the accumulation of excessive thioether groups within the COF pores, inducing the potential poisoning effect on Pt sites and resulting in the partial deactivation of subnanometric Pt particles, which is accordance with the observed experimental activity decreases for Pt@COF-S_x with the x ranging from 0.5 to 1.0. As a result, the amount of accessible Pt sites, showcasing a similar volcano-type curve to thioether content, might be responsible for the observed hydrogenation activity change over Pt@COF-S_x.

The above investigations illustrate that the formation of positively charged Pt surface, resulting from the interaction between thiols and Pt NPs, plays a crucial role in the selective hydrogenation of *p*-CNB. Drawing inspiration from these findings, it is expected that the treatment of conventional Pt nanoparticulate catalysts, such as commercial Pt/C, with thiols could serve as an effective strategy to producing highly selective catalysts aimed at generating *p*-CAN. Typically, through treating commercial Pt/C with propanethiol at 60 °C, the thiol-modified catalysts have been obtained, denoted as Pt/C-S_V (where V represents the volume of propanethiol; see SI, Experimental Section S2.3). Notably, the conversion can maintain > 99 % when V is less than 10 μL, but display a gradual decline with further increased modification (V > 10 μL, Figure 6), possibly attributed to the reduction in the number of accessible Pt sites. More importantly, the modified catalyst exhibits consistently high selectivity (> 99 %) towards *p*-CAN, which is significantly higher than the pristine Pt/C catalyst featuring poor selectivity of 41 % under the same conditions (Figure 6). The above results provide a successful demonstration, which shows the possibility of extending the idea on improved catalytic performance by microenvironment modulation from COF-based materials to other heteroge-

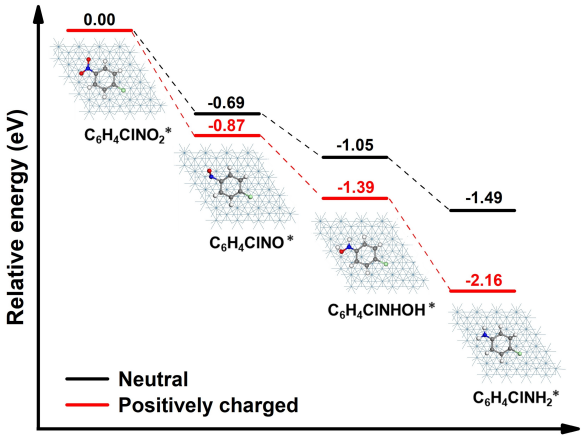

Figure 5. Relative energy variation along the reaction coordinate of the hydrogenation of *p*-CNB to *p*-CAN on neutral or positively charged Pt (111) surfaces.

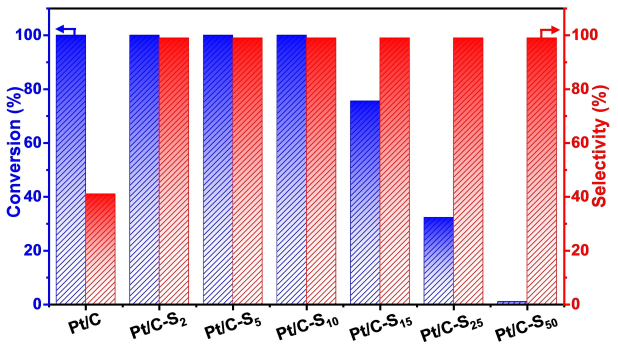

Figure 6. The hydrogenation conversion of *p*-CNB and selectivity to *p*-CAN over Pt/C-S_V. Reaction conditions: *p*-CNB (0.2 mmol), catalyst (10 mg), ethanol (5 mL), H_2 (1.5 MPa), 80 °C, 0.5 h.

© 2024 Wiley-VCH GmbH

15213773, 2024, 39, Downloaded from https://onlinelibrary.wiley.com/doi/10.1002/anie.202410097 by University Of Science, Wiley Online Library on [17/09/2024]. See the Terms and Conditions (https://onlinelibrary.wiley.com/terms-and-conditions) on Wiley Online Library for rules of use; OA articles are governed by the applicable Creative Commons License

neous catalysts, even commercial Pt/C, for promoted catalysis by simple post-treatment.

Conclusion

In brief, we have successfully fabricated a series of Pt@COF-S_x composites, in which Pt NPs are surrounded with the unique microenvironment composed by engineered thioether groups on the COF pore wall, allowing for precise control over the properties of the encapsulated Pt NPs. This particular microenvironment around Pt NPs has been demonstrated to be crucial in the hydrogenation of *p*-CNB over Pt@COF-S_x, which exhibit almost absolute selectivity to *p*-CAN, in stark contrast to the low selectivity over Pt NPs incorporated in the thioether-free COFs. Furthermore, a fascinating volcano-type curve has been observed in the conversion rates along with incremental thioether content, which can be attributed to the number change of accessible Pt sites. This work provides a rational means to regulate catalytic performance of supported metal NPs by microenvironment modulation; specifically, precise pore wall engineering of host COFs, offers a promising strategy for supported catalysts toward improved performance.

Acknowledgements

This work was supported by the National Key Research and Development Program of China (2021YFA1500402), the National Natural Science Foundation of China (22331009, U22A20401, 22205224), the Strategic Priority Research Program of the Chinese Academy of Sciences (XDB0450302, XDB0540000), and Fundamental Research Funds for the Central Universities (WK2060000038). The calculations in this work are supported by the Supercomputing Center of University of Science and Technology of China (USTC) and Hefei Advanced Computing Center. This work was partially carried out at the Instruments Center for Physical Science, USTC.

Conflict of Interest

The authors declare no conflict of interest.

Data Availability Statement

The data that support the findings of this study are available from the corresponding author upon reasonable request.

Keywords: Covalent Organic Framework · Heterogeneous Catalysis · Selective Hydrogenation · Metal Nanoparticles · Microenvironment Modulation

[1] a) S. Kattel, P. J. Ramírez, J. G. Chen, J. A. Rodriguez, P. Liu, *Science* **2017**, *355*, 1296–1299; b) K. Cheng, L. C. J. Smulders, L. I. V. D. Wal, J. Oenema, J. D. Meeldijk, N. L. Visser, G. Sunley, T. Roberts, Z. Xu, E. Doskocil, H. Yoshida, Y. Zheng, J. Zecevic, P. T. D. Jongh, K. P. D. Jong, *Science* **2022**, *377*, 204–208.

[2] a) Q.-L. Zhu, Q. Xu, *Chem* **2016**, *1*, 220–245; b) J. H. Swisher, L. Jibril, S. H. Petrosko, C. A. Mirkin, *Nat. Rev. Mater.* **2022**, *7*, 428–448.

[3] a) L. Zhang, M. Zhou, A. Wang, T. Zhang, *Chem. Rev.* **2020**, *120*, 683–733; b) K. Liu, R. Qin, N. Zheng, *J. Am. Chem. Soc.* **2021**, *143*, 4483–4499.

[4] a) Q. Wang, D. Astruc, *Chem. Rev.* **2020**, *120*, 1438–1511; b) Q. Zhang, S. Gao, J. Yu, *Chem. Rev.* **2023**, *123*, 6039–6106; c) Q. Yang, Q. Xu, H.-L. Jiang, *Chem. Soc. Rev.* **2017**, *46*, 4774–4808; d) L. Liu, A. Corma, *Nat. Rev. Mater.* **2021**, *6*, 244–263.

[5] a) A. P. Cote, A. I. Benin, N. W. Ockwig, M. O'Keeffe, A. J. Matzger, O. M. Yaghi, *Science* **2005**, *310*, 1166–1170; b) K. Geng, T. He, R. Liu, S. Dalapati, K. T. Tan, Z. Li, S. Tao, Y. Gong, Q. Jiang, D. Jiang, *Chem. Rev.* **2020**, *120*, 8814–8933; c) J. Han, J. Feng, J.-M. Chen, X.-Y. Du, S.-Y. Ding, L. Liang, W. Wang, *Science* **2024**, *383*, 1014–1019; d) D. W. Burke, R. R. Dasari, V. K. Sangwan, A. K. Oanta, Z. Hirani, C. E. Pelkowski, Y. Tang, R. Li, D. C. Ralph, M. C. Hersam, S. Barlow, S. R. Marder, W. R. Dichtel, *J. Am. Chem. Soc.* **2023**, *145*, 11969–11977; e) Q. Zhang, S. Dong, P. Shao, Y. Zhu, Z. Mu, D. Sheng, T. Zhang, X. Jiang, R. Shao, Z. Ren, J. Xie, X. Feng, B. Wang, *Science* **2022**, *378*, 181–186; f) W. Zhang, L. Chen, S. Dai, C. Zhao, C. Ma, L. Wei, M. Zhu, S. Y. Chong, H. Yang, L. Liu, Y. Bai, M. Yu, Y. Xu, X.-W. Zhu, Q. Zhu, S. An, R. S. Sprick, M. A. Little, X. Wu, S. Jiang, Y. Wu, Y.-B. Zhang, H. Tian, W.-H. Zhu, A. I. Cooper, *Nature* **2022**, *604*, 72–79; g) S. Zhang, G. Cheng, L. Guo, N. Wang, B. Tan, S. Jin, *Angew. Chem. Int. Ed.* **2020**, *59*, 6007–6014; h) D. H. Streater, E. R. Kennehan, D. Wang, C. Fiankor, L. Chen, C. Yang, B. Li, D. Liu, F. Ibrahim, I. Hermans, K. L. Kohlstedt, L. Luo, J. Zhang, J. Huang, *J. Am. Chem. Soc.* **2024**, *146*, 4489–4499; i) Z. Alsudairy, N. Brown, C. Yang, S. Cai, F. Akram, A. Ambus, C. Ingram, X. Li, *Precis. Chem.* **2023**, *1*, 233–240; j) Y. Yang, X. Chu, H.-Y. Zhang, R. Zhang, Y.-H. Liu, F.-M. Zhang, M. Lu, Z.-D. Yang, Y.-Q. Lan, *Nat. Commun.* **2023**, *14*, 593.

[6] L. Liu, A. Corma, *Chem. Rev.* **2018**, *118*, 4981–5079.

[7] a) X. Li, C. Zhang, S. Cai, X. Lei, V. Altoe, F. Hong, J. J. Urban, J. Ciston, E. M. Chan, Y. Liu, *Nat. Commun.* **2018**, *9*, 2998; b) X. Guan, Q. Fang, Y. Yan, S. Qiu, *Acc. Chem. Res.* **2022**, *55*, 1912–1927; c) T. Zhang, G. Zhang, L. Chen, *Acc. Chem. Res.* **2022**, *55*, 795–808; d) T. He, R. Liu, S. Wang, I. Keng W On, Y. Wu, Y. Xing, W. Yuan, J. Guo, Y. Zhao, *J. Am. Chem. Soc.* **2023**, *145*, 18015–18021.

[8] a) M. Guo, S. Jayakumar, M. Luo, X. Kong, C. Li, H. Li, J. Chen, Q. Yang, *Nat. Commun.* **2022**, *13*, 1770; b) S. Lu, Y. Hu, S. Wan, R. McCaffrey, Y. Jin, H. Gu, W. Zhang, *J. Am. Chem. Soc.* **2017**, *139*, 17082–17088; c) Y. Deng, Z. Zhang, P. Du, X. Ning, Y. Wang, D. Zhang, J. Liu, S. Zhang, X. Lu, *Angew. Chem. Int. Ed.* **2020**, *59*, 6082–6089; d) H.-C. Ma, C.-C. Zhao, G.-J. Chen, Y.-B. Dong, *Nat. Commun.* **2019**, *10*, 3368; e) M. Guo, Q. Meng, W. Chen, Z. Meng, M. Gao, Q. Li, X. Duan, H.-L. Jiang, *Angew. Chem. Int. Ed.* **2023**, *62*, e202305212.

[9] C. Kang, Z. Zhang, A. K. Usadi, D. C. Calabro, L. S. Baugh, K. Chai, Y. Wang, D. Zhao, *J. Am. Chem. Soc.* **2022**, *144*, 20363–20371.

[10] Q. Sun, B. Aguila, J. Perman, L. D. Earl, C. W. Abney, Y. Cheng, H. Wei, N. Nguyen, L. Wojtas, S. Ma, *J. Am. Chem. Soc.* **2017**, *139*, 2786–2793.

[11] W. Wan, J. Geiger, N. Berdunov, M. L. Luna, S. W. C. N. Daelman, N. López, S. Shaikhutdinov, B. R. Cuenya, *Angew. Chem. Int. Ed.* **2022**, *61*, e202112640.

[12] a) C. P. O'Brien, G. R. Jenness, H. Dong, D. G. Vlachos, I. C. Lee, *J. Catal.* **2016**, *337*, 122–132; b) X. I. Pereira-Hernández,

© 2024 Wiley-VCH GmbH

15213773, 2024, 39, Downloaded from https://onlinelibrary.wiley.com/doi/10.1002/anie.202410097 by University Of Science, Wiley Online Library on [17/09/2024]. See the Terms and Conditions (https://onlinelibrary.wiley.com/terms-and-conditions) on Wiley Online Library for rules of use; OA articles are governed by the applicable Creative Commons License

A. DeLaRiva, V. Muravev, D. Kunwar, H. Xiong, B. Sudduth, M. Engelhard, L. Kovarik, E. J. M. Hensen, Y. Wang, A. K. Datye, *Nat. Commun.* **2019**, *10*, 1358.

[13] a) R. V. Jagadeesh, A.-E. Surkus, H. Junge, M.-M. Pohl, J. Radnik, J. Rabeah, H. Huan, V. Schünemann, A. Brückner, M. Beller, *Science* **2013**, *342*, 1073–1076; b) J. Zhang, L. Wang, Y. Shao, Y. Wang, B. C. Gates, F.-S. Xiao, *Angew. Chem. Int. Ed.* **2017**, *56*, 9747–9751; c) L. Lin, S. Yao, R. Gao, X. Liang, Q. Yu, Y. Deng, J. Liu, M. Peng, Z. Jiang, S. Li, Y.-W. Li, X.-D. Wen, W. Zhou, D. Ma, *Nat. Nanotechnol.* **2021**, *12*, 1358; d) Z. Wang, C. Wang, S. Mao, B. Lu, Y. Chen, X. Zhang, Z. Chen, Y. Wang, *Nat. Commun.* **2022**, *12*, 3561; e) L. Li, Z. Li, W. Yang, Y. Huang, G. Huang, Q. Guan, Y. Dong, J. Lu, S.-H. Yu, H.-L. Jiang, *Chem* **2021**, *7*, 686–698.

[14] a) F. Yang, H. Yu, C. Wu, S. Wang, T. Li, H. Yin, *ACS Appl. Nano Mater.* **2022**, *5*, 11627–11635; b) J. Li, S. Ding, F. Wang, H. Zhao, J. Kou, M. Akram, M. Xu, W. Gao, C. Liu, H. Yang, Z. Dong, *J. Colloid Interface Sci.* **2022**, *625*, 640–650.

[15] J. Lyu, J. Wang, C. Lu, L. Ma, Q. Zhang, X. He, X. Li, *J. Phys. Chem. C* **2014**, *118*, 2594–2601.

[16] a) L. Liu, M. Lopez-Haro, C. W. Lopes, S. Rojas-Buzo, P. Concepcion, R. Manzorro, L. Simonelli, A. Sattler, P. Serna, J. J. Calvino, A. Corma, *Nat. Catal.* **2020**, *3*, 628–638; b) M. Xu, X. Qin, Y. Xu, X. Zhang, L. Zheng, J.-X. Liu, M. Wang, X. Liu, D. Ma, *Nat. Commun.* **2022**, *13*, 6720.

Manuscript received: May 28, 2024
Accepted manuscript online: July 2, 2024
Version of record online: August 19, 2024

© 2024 Wiley-VCH GmbH

15213773, 2024, 39, Downloaded from https://onlinelibrary.wiley.com/doi/10.1002/anie.202410097 by University Of Science, Wiley Online Library on [17/09/2024]. See the Terms and Conditions (https://onlinelibrary.wiley.com/terms-and-conditions) on Wiley Online Library for rules of use; OA articles are governed by the applicable Creative Commons License